Automatic phasing of MR images. Part I: Linearly varying phase

G. Larry Bretthorst *

Biomedical Magnetic Resonance Laboratory, Department of Radiology, Washington University, Campus Box 8227, 525 Scott Avenue, Suite 2313, St. Louis, MO 63110, USA

Abstract

In spin-echo and well shimmed gradient-echo images, the phase of the complex image often varies linearly in both the readout and phase-encode directions. Thus, in principle, it is possible to display an image in absorption mode. However, manually determining the two first-order and one zero-order phase parameters needed to display an absorption-mode image is a formidable task. In this paper, the Bayesian calculations needed to automatically determine these parameters are presented, and the calculations are illustrated using spin-echo images.

© 2008 Elsevier Inc. All rights reserved.

Keywords: Absorption-mode images; Zero- and first-order phase estimation; Frequency estimation; Bayesian probability theory

1. Introduction

Absorption-mode images, the real part of an appropriately phased discrete Fourier transform, have significant advantages over absolute-value images, including: increased signal-to-noise ratio, elimination of the correlations between the signal and the noise, elimination of the constant offset, preservation of the sign of the magnetization and preservation of the k-space noise properties. In addition, absorption-mode images are sharper than the corresponding absolute-value images. For images in which the phase varies linearly in both the phase-encode and readout domains, three parameters are needed to produce an absorption-mode image: two first-order and one zero-order phase parameters. In this paper, Bayesian probability theory [1–6] is used to estimate these three phase parameters.

The literature is modest with respect to the problem of generating absorption-mode images. There are many papers that address phasing one-dimensional NMR spectra [7–14] and several papers that address phasing multi-dimensional NMR spectra [15,16]. However, only four papers were found that directly address the problem of generating absorption-mode images, [17–20]. Of the four papers, two [17,18] used a zero-order and a *single* first-order phase parameter to generate the absorption-mode image. The techniques described in these papers are not adequate to phase MR images in which the phase is a linear function in both the readout and phase-encode directions. Liu et al. [19] recognized this problem and updated their algorithm to include all of the necessary phase parameters. However, they estimated the first-order phase parameters from the derivative of the image phase, which requires simultaneous estimation of derivatives and solving the phase unwrapping problem. The most recent paper [20] is concerned with echo-planer spectroscopic imaging for which the zero- and first-order phase parameters were determined using a nonlinear optimization procedure. In the image domain, this estimation problem is isomorphic to estimating a spatial frequency having unknown constant phase and a positionally dependent amplitude. Searching for this spatial frequency is similar to searching for the global maximum of a power spectrum. Unless good initial estimates of the first-order phase parameters are available, nonlinear optimization procedures may become stuck in local minima and yield nonoptimal phasing parameters.

* Fax: +1 314 362 0526.
E-mail address: gbretthorst@wustl.edu

2. Advantages of absorption-mode images

Fig. 1 shows an *ex vivo* spin-echo image of mouse brain acquired on a Varian NMR Systems 4.7-T scanner. The matrix size is 128×128 with a field of view of 2 cm by 2 cm. The voxel volume is $0.15\,\text{mm}^3$ with $TE = 55$ ms and $TR = 3100$ ms. The left-hand panels relate to absorption-mode images, while the right-hand panels relate to absolute-value mode images. Fig. 1c is an absorption-mode image of these data; while Fig. 1f is the same image displayed in absolute-value mode. The top two panels, (a) and (d), are traces through the noise in the respective images. While the center two panels, (b) and (e), are traces through the mouse brain. The location of the four traces are indicated by the solid lines, one white and one black, on each image. The axes in these traces are drawn through zero intensity.

In panel (a), a noise trace in the absorption-mode image, the noise oscillates around zero and is uncorrelated. The noise is uncorrelated because the discrete Fourier transform is a linear operator, and if the noise is uncorrelated in k-space, it remains uncorrelated in the image domain, provided a nonzero padded discrete Fourier transform was used to generate the image. However, in the absolute-value mode image, the noise fluctuates around a positive offset. This is illustrated in panels (d) and (e) where the axis marks the location of zero intensity. The size of this offset is roughly $\sqrt{\pi/2}\,\sigma$, the mean of the Rayleigh distribution, where σ is the standard deviation of the noise in the absorption-mode image. Additionally, in regions where there is signal, these fluctuations are correlated with the signal intensity. To illustrate this, if S_R and S_I represent the real and imaginary image signal components in a given voxel, and if n_R and n_I represent the image noise, then the absolute value of this image voxel is given by $\sqrt{(S_R + n_R)^2 + (S_I + n_I)^2}$, and terms of the form $2S_R n_R$ and $2S_I n_I$ are always present.
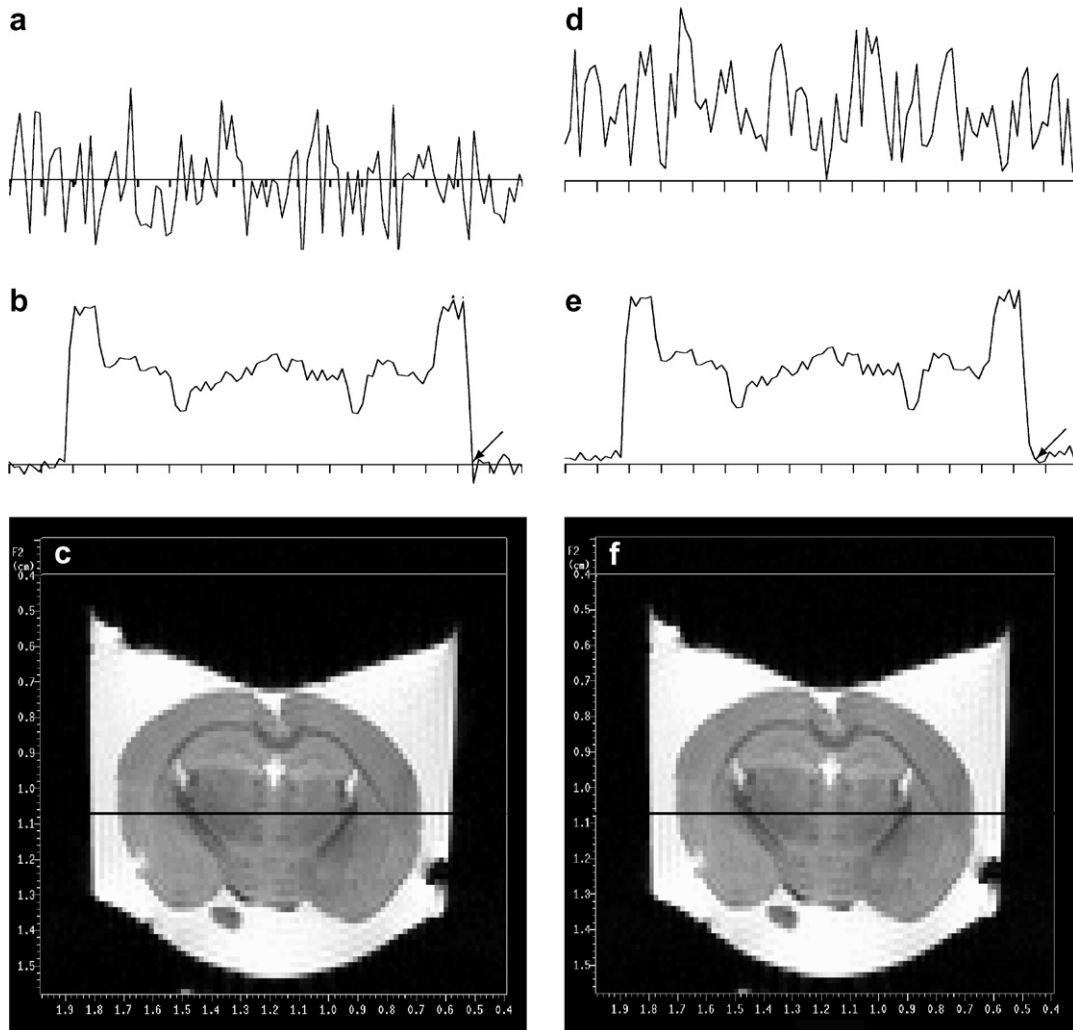

Fig. 1. *Ex vivo* images of mouse brain in formalin. The left-hand side of this figure relates to absorption-mode images, while the right-hand side, relates to absolute-value images. (c and f) Absorption and absolute-value mode images, respectively. The upper two traces, (a) and (d) are traces through the noise, while the middle two traces, (b) and (e) are through the brain. The arrows in (b) and (e) highlight the subtle difference in the sharpness of the absorption-mode images when compared to absolute-value images.

The use of absorption-mode images has other beneficial effects. For example, Fig. 1 shows one image from an inversion recovery sequence. If one phases the fully recovered data set and then applies those same phases to the other images in this sequence, the images will recover from negative to positive values; thus maintaining the correct sign of the magnetization.

Examination of the area around the arrows in panels (b) and (e) reveals that the absorption-mode image is sharper than the absolute-value image. This sharpening is not as pronounced as the sharpening of MR spectroscopic absorption lines because the k-space data do not relax appreciably due to T_2 over the time needed to acquire them.

Fig. 1 panels (a) and (d) provides a comparison of the noise present in absorption-mode verses absolute-value mode images. Note that the peak-to-peak variation of the noise in the absolute-value mode image is smaller than the peak-to-peak variation of the noise in the absorption-mode image, 0.19 and 0.30, respectively. This accounts for the somewhat smoother appearance of absolute-value images. However, the noise in the absolute-value mode image is not the peak-to-peak variation, rather it is the root mean-square of all of the signal in the noise regions, *including* the offset. This value, 0.43, is larger than the peak-to-peak variation in the absorption-mode image by a factor of almost exactly a $\sqrt{2}$. This $\sqrt{2}$ comes about because, on average, both the real and imaginary parts of the image contribute 0.3^2 to the noise power. The noise in the absorption-mode image has zero offset, while the noise in the absolute-value mode data has a substantial offset (0.37). This offset is noise dependent and may have undesirable effects on image analysis. For example, the estimated decay rate constant for T_2 relaxation data using absolute-value images gives relaxation rates that are too small because parameter estimation procedures fit all of the data *including* the constant offset, thus causing the exponential to decay too slowly. Similar affects are present in the parameter estimates using diffusion tensor data.

3. The model

In Bayesian probability theory, the first step in any calculation is to relate the parameters of interest to the available data. To produce an absorption-mode image, there are three parameters that must be determined, one zero-order phase, θ, and two first-order phase parameters, τ_x and τ_y. In k-space these first-order phase parameters are the centers of the echos in the readout and phase-encode directions, and they will be referred to as time delays. These time delays are on the order of one half the acquisition time, i.e., the peak of the echo is near the center of the acquisition window. Consequently, these delays cause the phase in the complex image to vary by approximately 180° every other voxel in the image, Fig. 2. The trace shown in Fig. 2 is the same one shown in Fig. 1b, before the phase parameters were applied. This oscillation can
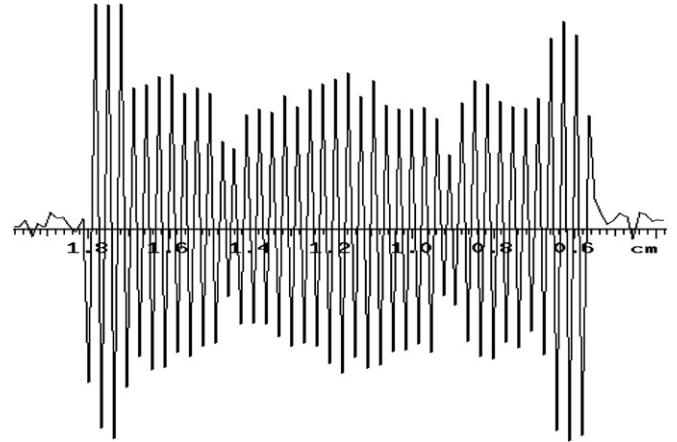

Fig. 2. The same trace shown in Fig. 1b before the effects of the linear and constant phase were removed. In a typical MR image the echos are centered in the acquisition time. In the image domain, this time delay corresponds to a spatial frequency which oscillate roughly every other point in the image.

be mitigated somewhat by using a time shift before the discrete Fourier transform is performed. Some spectrometer manufacturers do this, others do not; regardless, the parameter estimation problem remains unchanged by shifting the origin of time.

In the image domain, the data look like a sinusoid having an unknown spatial frequency, a positionally dependent amplitude and a constant phase. If this image domain model is used, the corresponding complex k-space model is an orthogonal Fourier series:

$$d_{ji} = \sum_{k=1}^{N_x} B_{jk} \exp\{ix_k(t_{xi} + \tau_x) + i\theta_j\} + n_{ji} \tag{1}$$

where the ith complex data value of the jth phase-encode is designated as d_{ji}, the kth Fourier expansion coefficient of the jth phase-encode is designated as B_{jk} and the constant phase for this phase-encode is θ_j. In dimensionless units, the spatial frequencies, x_k, run from zero to 2π in steps of $2\pi/N_x$, and the times, t_{xi}, are data point numbers, 0, 1, 2, etc. Finally, n_{ji} represents the ith complex noise value in the jth phase-encode. Separating Eq. (1) into its real and imaginary parts, one has

$$d_{Rji} = \sum_{k=1}^{N_x} B_{jk} M_{Rjki} + n_{Rji} \tag{2}$$

for the real data d_{Rji}, and

$$d_{Iji} = \sum_{k=1}^{N_x} B_{jk} M_{Ijki} + n_{Iji} \tag{3}$$

for the imaginary data d_{Iji}, where n_{Rji} and n_{Iji} represent the real and imaginary noise components. The two model functions, M_{Rjki} and M_{Ijki}, are given by

$$M_{Rjki} \equiv \cos(\theta_j)\cos(x_k[t_{xi} + \tau_x]) - \sin(\theta_j)\sin(x_k[t_{xi} + \tau_x]) \tag{4}$$

and

$$M_{Ijki} \equiv \cos(\theta_j)\sin(x_k[t_{xi} + \tau_x]) + \sin(\theta_j)\cos(x_k[t_{xi} + \tau_x]). \tag{5}$$

To obtain the posterior probability for τ_y, the role of x and y are simply exchanged in the posterior probability for τ_x. Consequently, we do not give the model relating τ_y to the k-space data.

4. The Bayesian calculations

The purpose of this paper is to obtain a set of point estimates for the three parameters, τ_x, τ_y and θ, and to use these point estimates to generate absorption-mode images. Bayesian probability theory is used to derive the posterior probability for these three parameters. The posterior probability for the time delays, τ_x and τ_y, are derived in this paper. The point estimates for these delays are obtained by locating the maximum of their posterior probabilities. In the case of the constant phase, θ, an exact expression for the maximum of its posterior probability is given. However, the derivation of this posterior probability and its point estimate are given in a companion paper [22].

In Bayesian probability theory, everything known about τ_x is summarized in a probability density function. This posterior probability density function is designated as $P(\tau_x | DI)$, which is read as the posterior probability for τ_x given all of the data D and the prior information I. The prior information I is all of the information used to make this a well-posed problem, including the specification of the model and the information used in assigning the various probabilities. The posterior probability for τ_x is computed by application of Bayes' theorem [1]:

$$P(\tau_x | DI) = \frac{P(\tau_x | I)P(D | \tau_x I)}{P(D | I)}, \tag{6}$$

where $P(\tau_x | I)$ is the prior probability for τ_x and represents what is known about τ_x before collecting the data, $P(D | \tau_x I)$ is the direct probability for the data given τ_x and represents what was learned from the data, and $P(D | I)$ is the direct probability for the data given only the prior information. In parameter estimation problems, $P(D | I)$ is a normalization constant and can be dropped provided the posterior probability is normalized at the end of the calculation. Dropping $P(D | I)$ one obtains

$$P(\tau_x | DI) \propto P(\tau_x | I)P(D | \tau_x I). \tag{7}$$

The direct probability for the data given τ_x, $P(D | \tau_x I)$, is a marginal probability from which one or more hypotheses have been removed by application of the sum and product rules. In this particular case, the Fourier expansion coefficients, the phases and the standard deviation of the noise prior probabilities have all been removed by marginalization. Reintroducing these quantities and applying the sum rule, one obtains

$$P(\tau_x | DI) \propto P(\tau_x | I) \int dBd\Theta d\sigma P(B\Theta\sigma D | \tau_x I), \tag{8}$$

where B, Θ and σ represent *all* of the Fourier expansion coefficients, phases and noise standard deviations in the model, Eq. (1). The right-hand side of this equation is factored using the product rule:

$$P(\tau_x | DI) \propto P(\tau_x | I) \int dBd\Theta d\sigma P(B | I)P(\Theta | I)$$
$$\times P(\sigma | I)P(D | B\Theta\sigma\tau_x I), \tag{9}$$

where probabilities of the form $P(\cdot | I)$ are prior probabilities for the respective parameters, and $P(D | B\Theta\sigma\tau_x I)$ is the direct probability for the data given the parameters.

In estimating the value of τ_x, the data may be thought of as N_y different data sets, each bearing on the value of τ_x. Since each phase-encode is an independent measurement, the direct probability for all the data, $P(D | B\Theta\sigma\tau_x I)$, is the product of the direct probabilities computed from each line in k-space separately. Similarly, the prior probabilities for the Fourier expansion coefficients are the products of the prior probabilities for the Fourier expansion coefficients in each line of k-space. Factoring the posterior probability for τ_x, one obtains

$$P(\tau_x | DI) \propto P(\tau_x | I) \prod_{j=1}^{N_y} \int dB_{j1} \dots dB_{jN_x} d\theta_j d\sigma_j$$
$$\times [P(\theta_j | I)P(\sigma_j | I) \times P(B_{j1} \dots B_{jN_x} | I)$$
$$\times P(D_j | B_{j1} \dots B_{jN_x}\theta_j\sigma_j I)], \tag{10}$$

where logical independence of the parameters is assumed. Additionally, some spectrometer manufacturers use filters that are not flat over the entire image. Consequently, the noise standard deviation, σ_j, is positionally dependent. The joint prior probability for the Fourier expansion coefficients in the jth phase-encode, $P(B_{j1} \dots B_{jN_x} | I)$, has not been factored because a correlated prior for these expansion coefficients will be assigned.

Numerical values must now be assigned to represent each of the probabilities. The prior probability for the time delay, $P(\tau_x | I)$, will be assigned using a uniform prior probability:

$$P(\tau_x | I) = \begin{cases} \frac{2}{N_x} & \text{if } N_x/4 \leqslant \tau_x \leqslant 3N_x/4 \\ 0 & \text{otherwise} \end{cases}, \tag{11}$$

where the prior ranges express the fact that outside of the valid range the likelihood is aliased as a function of τ_x.

The prior probability for the standard deviation, $P(\sigma_j | I)$, is assigned a Jeffreys' prior [2]

$$P(\sigma_j | I) \propto \frac{1}{\sigma_j}. \tag{12}$$

The prior probability for the phase, $P(\theta_j | I)$, is assigned using a uniform prior probability:

$$P(\theta_j | I) = \begin{cases} \frac{1}{2\pi} & \text{if } 0 \leqslant \theta_j \leqslant 2\pi \\ 0 & \text{otherwise} \end{cases}. \tag{13}$$

The prior probability for the Fourier expansion coefficients, $P(B_{j1} \ldots B_{jN_x} \mid I)$, is assigned as a generalized Gaussian. This generalized Gaussian will be written as:

$$P(B_{j1} \ldots B_{jN_x} \mid \beta I) \propto \sigma_j^{-N_x} \exp \left\{ -\frac{\beta^2}{2\sigma_j^2} \sum_{k=1}^{N_x} \sum_{l=1}^{N_x} B_{jl} \mathbf{U}_{kl} B_{jk} \right\}, \tag{14}$$

where several constant factors that cancel when the posterior probability density function is normalized have been dropped. The matrix, $\mathbf{U}_{kl}$, specifies how the Fourier expansion coefficients are related to each other. In the program that implements this calculation, the matrix $\mathbf{U}_{kl}$ is tridiagonal, having $[-1, 2, -1]$ as its three nonzero diagonals. This tridiagonal matrix expresses the belief that adjacent voxels should be approximately equal. The parameter β expresses how strongly this is believed. In the calculations that follow, it is the Gaussian form of this prior that is important, not the individual components of this matrix.

If the direct probability for the jth phase-encode, $P(D_j \mid B_{j1} \ldots B_{jN_x} \theta_j \sigma_j I)$, is assigned using a Gaussian noise prior probability for the real and imaginary noise components, the joint posterior probability for τ_x, Eq. (10), can then be written as:

$$P(\tau_x \mid DI) \propto \prod_{j=1}^{N_y} \int d\theta_j d\sigma_j dB_{j1} \ldots dB_{jN_x}$$
$$\times \sigma_j^{-3N_x - 1} \exp \left\{ -\frac{Q_j}{2\sigma_j^2} \right\}, \tag{15}$$

where several constants that cancel when this distribution is normalized have been dropped. The quantity Q_j is given by

$$Q_j \equiv \sum_{k=1}^{N_x} \sum_{l=1}^{N_x} \beta^2 B_{jl} \mathbf{U}_{kl} B_{jk}$$
$$+ \sum_{i=1}^{N_x} \left(d_{Rji} - \sum_{k=1}^{N_x} B_{jk} M_{Rjki} \right)^2$$
$$+ \sum_{i=1}^{N_x} \left(d_{Iji} + \sum_{k=1}^{N_x} B_{jk} M_{Ijki} \right)^2. \tag{16}$$

The first line in this equation results from the prior probability for the Fourier expansion coefficients; the second and third lines are essentially χ^2 evaluated for the real and imaginary parts of the jth phase-encode.

Substituting the definitions of M_{Rjki} and M_{Ijki}, Eqs. (4) and (5), respectively into Eq. (16), one obtains

$$Q_j \equiv 2N_x \overline{d_{xj}^2} - 2 \sum_{l=1}^{N_x} B_{jl} T_{jl} + \sum_{l=1}^{N_x} \sum_{k=1}^{N_x} B_{jl} \mathbf{V}_{kl} B_{jk} \tag{17}$$

where T_{jl} is given by

$$T_{jl} \equiv F_{Rjl} \cos \theta_j + F_{Ijl} \sin \theta_j, \tag{18}$$

and can be computed from the real and imaginary parts of the discrete Fourier transform of the jth phase-encode. The interaction matrix, $\mathbf{V}_{kl}$, is given by

$$\mathbf{V}_{kl} \equiv N_x \delta_{kl} + \beta^2 \mathbf{U}_{kl}, \tag{19}$$

where δ_{kl} is a Kronecker delta function. The mean-square data value of the jth phase-encode, $\overline{d_{xj}^2}$, is defined as

$$\overline{d_{xj}^2} \equiv \frac{1}{2N_x} \sum_{i=1}^{N_x} (d_{Rxji}^2 + d_{Ixji}^2). \tag{20}$$

Finally, F_{Rjl} and F_{Ijl}, the projection of the real and imaginary parts of the model onto the data, are given by

$$F_{Rjl} \equiv \sum_{i=1}^{N_x} [d_{Rji} \cos(x_l[t_{xi} + \tau_x]) - d_{Iji} \sin(x_l[t_{xi} + \tau_x])] \tag{21}$$

and

$$F_{Ijl} \equiv \sum_{i=1}^{N_x} [d_{Rji} \sin(x_l[t_{xi} + \tau_x]) + d_{Iji} \cos(x_l[t_{xi} + \tau_x])], \tag{22}$$

respectively. The functions F_{Rjl} and F_{Ijl} are essentially the real and imaginary parts of a time shifted discrete Fourier transform. To compress the notation, the time delays were not separated from the other parts of the Fourier transform. However, application of various trigonometric identities reduces these quantities to linear combinations of the real and imaginary parts of the discrete Fourier transform of the k-space data. If N_x is a power of 2, the fast discrete Fourier transform may be used to compute F_{Rjl} and F_{Ijl}; otherwise, the slow transform must be used.

The functional form of Q_j, Eq. (17), is quadratic in the B_{jk}, so the integrals over the B_{jk} in Eq. (15) are Gaussian quadrature integrals, where the limits of integration range from minus to plus infinity. Such integrals are easily evaluated and the results, but not the details, of evaluating these integrals are given:

$$P(\tau_x \mid DI) \propto \prod_{j=1}^{N_y} \int d\theta_j d\sigma_j \sigma_j^{-2N_x - 1}$$
$$\times \exp \left\{ -\frac{2N_x \overline{d_{xj}^2} - N_x \overline{h^2}(\theta_j, \tau_x)}{2\sigma_j^2} \right\}, \tag{23}$$

where

$$\overline{h^2}(\theta_j, \tau_x) \equiv \frac{1}{N_x} \sum_{l=1}^{N_x} \hat{B}_{jl} T_{jl}. \tag{24}$$

The $\hat{B}_{jl}$ are given by the solution to

$$\sum_{l=1}^{N_x} \mathbf{V}_{kl} \hat{B}_{jl} = F_{Rjk} \cos \theta_j + F_{Ijk} \sin \theta_j, \tag{25}$$

which, for convenience, is written as

$$\hat{B}_{jl} \equiv \hat{a}_{jl} \cos \theta_j + \hat{b}_{jl} \sin \theta_j, \tag{26}$$

where $\hat{a}_{j\ell}$ and $\hat{b}_{j\ell}$ are given by the inverse of the $\mathbf{V}_{k\ell}$ matrix dotted into the column vectors represented by $F_{\text{R}jk}$ and $F_{\text{I}jk}$, respectively.

To evaluate the integral over the phase, Eqs. (18) and (26) are substituted into Eq. (24) to obtain

$$\overline{h^2}(\theta_j, \tau_x) = \sum_{\ell=1}^{N_x}[F_{\text{R}j\ell}\hat{a}_{j\ell}\cos^2(\theta_j) + F_{\text{I}j\ell}\hat{a}_{j\ell}\cos(\theta_j)\sin(\theta_j) \\ + F_{\text{R}j\ell}\hat{b}_{j\ell}\cos(\theta_j)\sin(\theta_j) + F_{\text{I}j\ell}\hat{b}_{j\ell}\sin^2(\theta_j)]. \quad (27)$$

Using various trigonometric identities, this equation may be transformed into

$$\overline{h^2}(\theta_j, \tau_x) = U_j + \sqrt{W_j^2 + X_j^2}\cos(2\theta_j + \psi_j) \quad (28)$$

with

$$U_j \equiv \frac{1}{2}\sum_{\ell=1}^{N_x}[\hat{a}_{j\ell}F_{\text{R}j\ell} + \hat{b}_{j\ell}F_{\text{I}j\ell}], \quad (29)$$

$$W_j \equiv \frac{1}{2}\sum_{\ell=1}^{N_x}[\hat{a}_{j\ell}F_{\text{R}j\ell} - \hat{b}_{j\ell}F_{\text{I}j\ell}], \quad (30)$$

$$X_j \equiv \frac{1}{2}\sum_{\ell=1}^{N_x}[\hat{a}_{j\ell}F_{\text{I}j\ell} + \hat{b}_{j\ell}F_{\text{R}j\ell}] \quad (31)$$

and

$$\psi_j = \tan^{-1}\left(\frac{X_j}{W_j}\right). \quad (32)$$

If Eq. (28) is substituted into Eq. (23), the integrand is of the form $\exp\{\cos(\theta_j)\}$, the integral representation of the I_0 Bessel function. Evaluating this integral, one obtains

$$P(\tau_x \mid DI)$$
$$\propto \prod_{j=1}^{N_y}\int \text{d}\sigma_j\sigma_j^{-2N_x-1}\times \exp\left\{-\frac{2N_x\overline{d_{xj}^2} - U_j}{2\sigma_j^2}\right\} \\ \times I_0\left(\frac{\sqrt{W_j^2 + X_j^2}}{2\sigma_j^2}\right). \quad (33)$$

In this form, the integral over the standard deviation of the noise prior probability, σ_j, is not easily represented in closed form. Fortunately, near the location of the maximum, there is an approximation that is good to many decimal places. For large argument, the I_0 Bessel function is nearly exponential:

$$I_0(z) \approx \frac{\exp\{z\}}{\sqrt{2\pi z}}, \quad (34)$$

so Eq. (33) is very nearly equal to

$$P(\tau_x \mid DI) \approx \prod_{j=1}^{N_y}\int \text{d}\sigma_j\sigma_j^{-2N_x-1}\exp\left\{-\frac{\mathcal{V}_j}{2\sigma_j^2}\right\}, \quad (35)$$

with

$$\mathcal{V}_j \equiv 2N_x\overline{d_{xj}^2} - U_j - \sqrt{W_j^2 + X_j^2}, \quad (36)$$

where a term that is nearly constant over the high probability region has been dropped. In this form, the integral over the standard deviation is a gamma integral. Evaluating this integral, one obtains:

$$P(\tau_x \mid DI) \propto \prod_{j=1}^{N_y}[\mathcal{V}_j]^{-N_x}, \quad (37)$$

where a number of constant factors have been dropped. This probability density function is of the form of Student's t-distribution and this t-distribution is used to estimate τ_x.

As noted above, to compute the posterior probability for τ_y, $P(\tau_y \mid DI)$, one needs only exchange the roles of x and y in the above equations.

Finally, one needs to compute the posterior probability for the constant phase, $P(\theta \mid DI)$. This is a marginal posterior probability in which the Fourier expansion coefficients, standard deviation of the noise prior probability and the two delay times have been removed using the sum and product rules of probability theory. However, as illustrated in the next section, the delay times are so well determined that marginalizing over them does little more than constrain them to their maximum posterior probability estimates. Additionally, any program that implements this calculation will use a point estimate of the phase, not the posterior density. Fortunately, a point estimate is available that, given the delay times, returns the peak of the posterior probability for θ. The calculation of this posterior probability is essentially identical to the calculation just described, and we do not repeat those details here. Those interested in phase estimation can refer to [22]. The value of the phase that maximizes this posterior probability and its width are given by:

$$(\theta)_{\text{est}} = \theta_{\max} \pm \sqrt{\frac{8\sigma^2}{\sqrt{W^2 + X^2}}} \quad (38)$$

$$\theta_{\max} = -\frac{1}{2}\tan^{-1}\left(\frac{X}{W}\right), \quad (39)$$

where X and W are given by

$$X = 2\sum_{j=1}^{N_y}\sum_{\ell=1}^{N_x}F_{\text{R}j\ell}F_{\text{I}j\ell}, \quad (40)$$

and

$$W = \sum_{j=1}^{N_y}\sum_{\ell=1}^{N_x}[F_{\text{R}j\ell}^2 - F_{\text{I}j\ell}^2], \quad (41)$$

and $F_{\text{R}j\ell}$ and $F_{\text{I}j\ell}$ are the real and imaginary parts of the two-dimensional discrete Fourier transform of the complex k-space data *after* removing the effects of both linearly varying phases.

5. Discussion

Fig. 3 is the natural logarithm of the posterior probability for the delay times computed using the k-space data
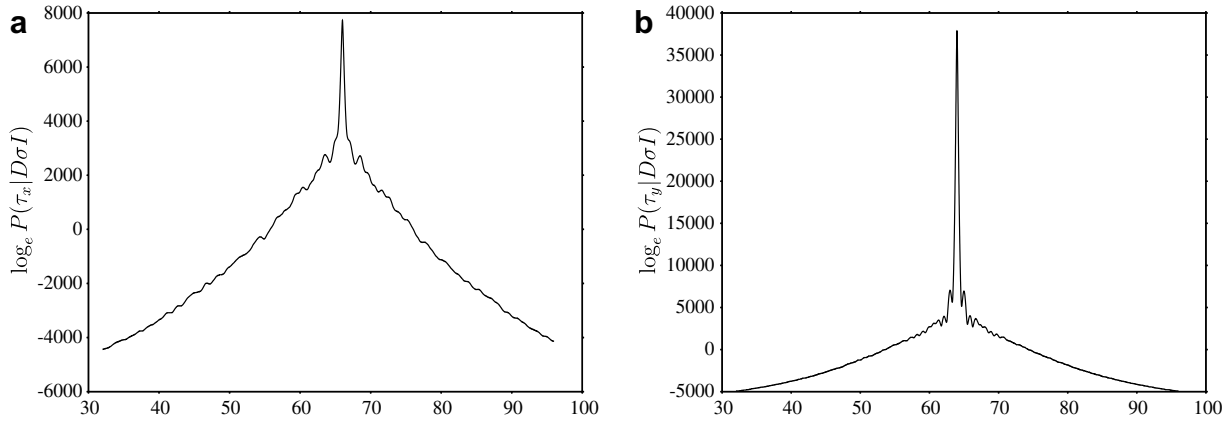
Fig. 3. The natural logarithm of the posterior probability for the delay times along both the readout direction (a), and in the phase-encode direction (b). These delay times are typically very well determined by the k-space data. In (b), the natural logarithm of $P(\tau_y \mid DI)$ goes through roughly 45,000 e-foldings.

shown in Fig. 1. The program that implements this calculation first computes the discrete Fourier transform in the readout direction and then uses this transform to compute the natural logarithm of the posterior probability for τ_x (Fig. 3a). In dimensionless units, τ_x varies from $N_x/4 \leqslant \tau_x \leqslant 3N_x/4$. The image shown in Fig. 1 contains $N_x = 128$ complex data values, so τ_x ranges from $32 \leqslant \tau_x \leqslant 96$. Outside of this range, the posterior probability for τ_x is aliased, and no additional information is available. Note that the logarithm, starts out low and increases from roughly -4000 to +8000. The reason the calculations are performed using the natural logarithm is simply that most computers cannot express this large of a dynamic range any other way. Fig. 3b is the natural logarithm of the posterior probability for τ_y. In the phase-encode direction, the logarithm of the posterior probability changes by about 45,000 e-foldings.

The values of both delays have been determined very precisely. To illustrate this, the fully normalized posterior probabilities for τ_x and τ_y are displayed in Fig. 4. In

Fig. 3 the full nonaliased range, $32 \leqslant \tau \leqslant 96$, for the delay times was plotted, while the plots shown in Fig. 4 span roughly 1/4300 and 1/9200 of the full nonaliased range. These distributions are plotted on the same vertical scale so that the difference in their widths, roughly a factor of 2.5, is more obvious. The mean and standard deviation estimate of τ_x and τ_y are given by

$$(\tau_x)_{\text{est}} = 66.0215 \pm 0.0025 \tag{42}$$

and

$$(\tau_y)_{\text{est}} = 63.9843 \pm 0.001 \tag{43}$$

respectively. In k-space, these uncertainties are in data point numbers. In the image domain, an uncertainty of 0.0025 data points, causes an accumulated phase uncertainty of only 0.016 radians (less than one degree) across the image. Consequently, the oscillations caused by the linearly varying phase are completely removed. The reason these delays are so precisely determined is a combination of signal-to-noise ratio and the number of data values.
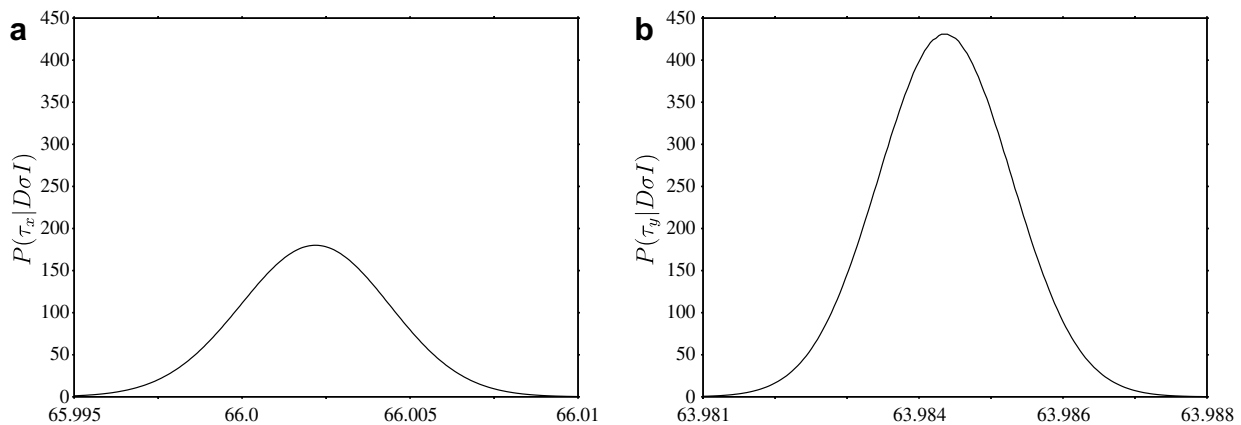

Fig. 4. (a and b) The fully normalized posterior probability for τ_x and τ_x, respectively. These posterior probabilities are plotted on the same vertical scale to illustrate that the standard deviation of the distribution shown in (a) is 2.5 times larger (0.0025 time units) than the standard deviation of the distribution shown in (b) (0.001 time units). Regardless, both echo centers are very precisely determined and, consequently, the linearly varying phase is very accurately canceled in the resulting absorption-mode image. For example, the uncertainty in echo center in the readout direction (a), causes an accumulated error in the phase of only 0.016 rad across the image.

A typically image has $128 \times 128 = 16,384$ data values. The uncertainty in the parameter estimates scales inversely with signal-to-noise ratio and inversely with the square root of the number of data values.

Similarly, the constant phase is also very well determined. For the data shown in Fig. 1c, the estimated value of the constant phase is

$$(\theta)_{\text{est}} = 24.346° \pm 0.002° \tag{44}$$

which means the error in constant phase is about one part in 12,000. The reason for this precision is again a combination of signal-to-noise ratio and total number of data values. In Eq. (38), the factor in the denominator of the square root (another square root) is essentially the total-squared signal intensity in the real and imaginary parts of the complex image. Consequently, that factor scales with both the number of complex data values and the average signal intensity. As a result, the uncertainty in the estimated phase varies inversely with the average signal-to-noise ratio and inversely with the square root of the total number of complex data values.

The program that implements this calculation computes the logarithm of the posterior probability for τ_x on a coarse grid, varying τ_x over its valid range in steps of 0.5. The value of τ_x that has the maximum posterior probability on this grid is saved. Using this maximum value, the logarithm of the posterior probability is then evaluated at $(\text{max} + 1/2)$ and $(\text{max} - 1/2)$. These three values of τ_x, and the three posterior probabilities, are used to bracket the maximum of the posterior probability. A one-dimensional search routine, similar to those described in [21], is used to find the value of τ_x that maximizes the posterior probability. Using the value of τ_x that maximized the posterior probability, the effect of the linear first-order phase is removed in the readout direction. The calculation is then repeated in the phase-encode direction, and these time delays are used to remove the effects of the linearly varying phase. Finally, the zero-order phase that has maximum posterior probability is computed, and its effect is then removed. The three parameter estimates given in Eqs. (42)–(44) are the values used to generate the absorption-mode image shown in Fig. 1c.

Because positivity was not imposed on the Fourier expansion coefficients, there is an ambiguity in the calculation of the zero-order phase, Eq. (39). If the calculated value of the zero-order phase is $\hat{\theta}$, the phase that gives positive intensities in the real channel can be either $\hat{\theta}$ or $\hat{\theta} + 180°$. Before removing the zero-order phase, the program does a calculation to determine which of these two phases is appropriate. This Bayesian calculation, not given, essentially repeats the calculation for the posterior probability for the zero-order phase given in [22] with an uncorrelated prior for the Fourier expansion coefficients that constrains these coefficients to be positive. This posterior probability is then evaluated for $\hat{\theta}$ and $\hat{\theta} + 180°$. Because the amplitudes are required to be positive, the phase that rotates the intensity to the real channel has

very high probability, while the phase that rotates the intensity to the imaginary channel has very low probability. Consequently, the phase with the highest posterior probability is used to remove the effects of the zero-order phase.

Finally, if the size of the desired image is different from the actual complex size of the k-space data, the final image is generated using a zero-padded discrete Fourier transform, and the image is phased using the three computed parameters.

6. Summary and conclusions

The advantages of absorption-mode vs. absolute-value mode images have been illustrated, and a Bayesian-based calculation has been described for generating absorption-mode images. These Bayesian calculations allow one to produce absorption-mode images using data in which the the phase of the image varies linearly as a function of position, as it does in most spin-echo images. In this lab, absorption-mode images are routinely produced on data sets containing thousands of images (DTI data sets with 48 directions and 60 to 70 slices are common). The calculations described in this paper have never failed to remove the effects of both the linearly varying and constant phases.

In cases for which the data have field inhomogeneity artifacts, as is common in gradient-echo images, the calculations presented here are used to remove the effects of both the linearly varying and constant phase and then the calculations described in [22] are used to remove the effects of the nonlinear varying phases to produce absorption-mode images. Additionally, the program that implements the calculation described in [22] produces an unwrapped map of the image phase. Because these are the phases that deviate from the expected linearly varying phase, the resulting unwrapped phase maps are essentially images of the magnetic field inhomogeneity.

The calculations presented in this paper are for 2D slice-selection data. Extending the calculations to 3D data requires one additional discrete Fourier transform and the estimation of a third delay time.

These calculations utilize the fact that the Fourier expansion is an orthogonal expansion, so they cannot be used on images in which the acquisition is not uniformly sampled in both domains. The calculations could be extended to nonuniformly sampled data, but said calculations would probably be computationally prohibitive due to the matrix inversion used in Eq. (26).

When the number of complex data in a given k-space data set are an integer power of 2, the fast discrete Fourier transform can be used to compute the projection of the data onto the model in that domain. Consequently, generating an absorption-mode image on a Sun Ultra 60 workstation requires less than a second. The calculations are roughly a factor of 2 slower when the number of complex data are not an integer power of 2.

Acknowledgments

References

[1] T. Bayes, Philos. Trans. R. Soc. Lond. 53 (1763) 370; reprinted in Rev. T. Bayes, Biometrika 45 (1958) 293, Facsimiles of Two Papers by Bayes, with commentary by W. Edwards Deming Hafner, New York, 1963.

[2] Sir H. Jeffreys, Theory of Probability, Oxford University Press, London, 1939, Later editions, 1948, 1961.

[3] R.T. Cox, Probability, frequency, and reasonable expectation, Am. J. Phys. 14 (1946) 1–13.

[4] R.T. Cox, The Algebra of Probable Inference, Johns Hopkins University Press, Baltimore MD, 1961.

[5] E.T. Jaynes, Probability theory—the logic of science, in: G.L. Bretthorst (Ed.), Cambridge University Press, Cambridge, UK, 2003.

[6] G.L. Bretthorst, Bayesian spectrum analysis and parameter estimation, in: J. Berger, S. Fienberg, J. Gani, K. Krickenberg, B. Singer (Eds.), Lecture Notes in Statistics, vol. 48, Springer-Verlag, New-York, 1988.

[7] R.R. Ernst, Numerical Hilbert transform and automatic phase correction in magnetic resonance spectroscopy, J. Magn. Reson. 1 (1969) 7–26.

[8] C.N. Chen, L.S. Kan, An iterative phase correction program for nuclear magnetic resonance (NMR) spectra, Comput. Methods Programs Biomed. 26 (1988) 81–84.

[9] L.F. Gladden, S.R. Elliott, A numerical phasing technique for application to one-dimensional NMR spectra, J. Magn. Reson. 68 (3) (1986) 383–388.

[10] D.E. Brown, T.W. Campbell, R.N. Moore, Automated phase correction of FT NMR spectra by baseline optimization, J. Magn. Reson. 85 (1989) 15–23.

[11] A. Heuer, A new algorithm for automatic phase correction by symmetrizing lines, J. Magn. Reson. 91 (1991) 241–253.

[12] D.E. Brown, Fully automated baseline correction of 1D and 2D NMR spectra using Bernstein polynomials, J. Magn. Reson. 114 (1995) 268–270.

[13] L. Chen, Z. Weng, L.Y. Goh, M. Garland, An efficient algorithm for automatic phase correction of NMR spectra based on entropy minimization, J. Magn. Reson. 158 (2002) 164–168.

[14] G. Stocha, Z. Olejniczak, Missing first points and phase artifact mutually entangled in FT NMR data—noniterative solution, J. Magn. Reson. 173 (2005) 140–152.

[15] R.E. Hoffman, F. Delaglio, G.C. Levy, Phase correction of two-dimensional NMR spectra using DISPA, J. Magn. Reson. 98 (1992) 231–237.

[16] R. Freeman, S.P. Kempsell, M.H. Levitt, Phase adjustment of two-dimensional NMR spectra, J. Magn. Reson. 34 (1979) 675–678.

[17] C.B. Anh, Z.H. Cho, A new phase correction method in NMR imaging based on autocorrelation and histogram analysis, IEEE Trans. Med. Imaging MI-6 (1987) 32–36.

[18] H.W. Park, M.H. Cho, Z.H. Cho, Real-value representation in inversionrecovery NMR imaging by use of a phase-correction method, J. Magn. Reson. Med. 3 (1) (1986) 15–23.

[19] J. Liu, J.L. Koenig, An automatic phase correction method in nuclear magnetic resonance imaging, J. Magn. Reson. 86 (1990) 593–604.

[20] S. Sarkar, K. Heberlein, G.J. Metzger, X. Zhang, X. Hu, Applications of high-resolution echoplanar spectroscopic imaging for structural imaging, J. Magn. Reson. Imag. 10 (1999) 1–7.

[21] W.H. Press, B.P. Flannery, S.A. Teukolsky, W.T. Vettering, Numerical Recipes: The Art of Scientific Computing, second ed., Cambridge University Press, Cambridge, 1992.

[22] G.L. Bretthorst, Automatic phasing of MR images. Part II: Voxel-wise phase estimation, J. Magn. Reson. 191 (2008) 193–201.